Biomedical Optics EXPRESS

Intraoperative handheld optical coherence tomography forward-viewing probe: physical performance and preliminary animal imaging

Cuiru Sun,[1] Kenneth K. C. Lee,[1,2] Barry Vuong,[1] Michael D. Cusimano,[3] Alexander Brukson,[4] Antonio Mauro,[5] Nigel Munce,[6] Brian K. Courtney,[7,8] Beau A. Standish,[1] and Victor X. D. Yang[1,2,*]

[1]Biophotonics and Bioengineering Laboratory, Department of Electrical and Computer Engineering, Ryerson University, 350 Victoria St. Toronto ON, M5B2K3 Canada
[2]Department of Electrical and Computer Engineering, University of Toronto, 27 King's College Circle, Toronto, Ontario, M5S 1A1, Canada
[3]Neurosurgery, St. Michael's Hospital, Li Ka Shing Building, 209 Victoria St, Toronto, ON, M5B 1T8, Canada
[4]Department of Biomedical Engineering, Ryerson University, 350 Victoria St. Toronto ON, M5B2K3 Canada
[5]Institute of Medical Science, University of Toronto, St. Michael's Hospital, 209 Victoria Street, Toronto, Ontario, M5B 1T8, Canada
[6]Faculty of Medicine, 1 King's College Circle, Toronto, ON, M5S 1A8, Canada
[7]Colibri Technologies Inc., 3080 Yonge Street, Toronto, ON, M4N 3N1, Canada
[8]Division of Cardiology, Sunnybrook Health Sciences Centre, 2075 Bayview Ave., Toronto, ON, M4N 3M5, Canada
**yangv@ee.ryerson.ca*

Abstract: A prototype intraoperative hand-held optical coherence tomography (OCT) imaging probe was developed to provide micron resolution cross-sectional images of subsurface tissue during open surgery. This new ergonomic probe was designed based on electrostatically driven optical fibers, and packaged into a catheter probe in the form factor of clinically accepted Bayonet shaped neurosurgical probes. Optical properties of the probe were measured to have a ~20 μm spot size, 5 mm working distance and 4 mm field of view. Feasibility of this probe for structural and Doppler shift imaging was tested on porcine femoral blood vessel imaging.

OCIS codes: (170.4500) Optical coherence tomography; (120.3890) Medical optics instrumentation

References and links

1. K. Hemminki, A. Försti, and J. G. Ji, "Incidence and familial risks in pituitary adenoma and associated tumors," Endocr. Relat. Cancer **14**(1), 103–109 (2007).
2. A. F. Daly, M. Rixhon, C. Adam, A. Dempegioti, M. A. Tichomirowa, and A. Beckers, "High prevalence of pituitary adenomas: a cross-sectional study in the province of Liege, Belgium," J. Clin. Endocrinol. Metab. **91**(12), 4769–4775 (2006).
3. W. G. Bradley, *Neurology in Clinical Practice*, 5th ed. (Butterworth-Heinemann/Elsevier, Philadelphia, PA, 2008), pp. 2, v, xvi, 2488, lxxx.
4. A. I. Qureshi, V. Janardhan, R. A. Hanel, and G. Lanzino, "Comparison of endovascular and surgical treatments for intracranial aneurysms: an evidence-based review," Lancet Neurol. **6**(9), 816–825 (2007).
5. M. Buchfelder, "Treatment of pituitary tumors: surgery," Endocrine **28**(1), 67–75 (2005).
6. E. Z. Kapsalaki, G. P. Lee, J. S. Robinson 3rd, A. A. Grigorian, and K. N. Fountas, "The role of intraoperative micro-Doppler ultrasound in verifying proper clip placement in intracranial aneurysm surgery," J. Clin. Neurosci. **15**(2), 153–157 (2008).
7. R. Stendel, T. Pietilä, A. A. Al Hassan, A. Schilling, and M. Brock, "Intraoperative microvascular Doppler ultrasonography in cerebral aneurysm surgery," J. Neurol. Neurosurg. Psychiatry **68**(1), 29–35 (2000).
8. P. Mortini and M. Giovanelli, "Transcranial approaches to pituitary tumors," Operative Tech. Neurosur. **5**(4), 239–251 (2002).
9. N. Fatemi, J. R. Dusick, M. A. de Paiva Neto, and D. F. Kelly, "The endonasal microscopic approach for pituitary adenomas and other parasellar tumors: a 10-year experience," Neurosurgery **63**(4 Suppl 2), 244–256, discussion 256 (2008).

#165607 - $15.00 USD Received 3 Apr 2012; revised 7 May 2012; accepted 8 May 2012; published 16 May 2012

10. J. R. Dusick, F. Esposito, D. Malkasian, and D. F. Kelly, "Avoidance of carotid artery injuries in transsphenoidal surgery with the Doppler probe and micro-hook blades," Neurosurgery **60**(4 Suppl 2), 322–328, discussion 328–329 (2007).
11. J. M. Schmitt, "Optical coherence tomography (OCT): A review," IEEE J. Sel. Top. Quantum Electron. **5**(4), 1205–1215 (1999).
12. V. X. D. Yang, N. Munce, J. Pekar, M. L. Gordon, S. Lo, N. E. Marcon, B. C. Wilson, and I. A. Vitkin, "Micromachined array tip for multifocus fiber-based optical coherence tomography," Opt. Lett. **29**(15), 1754–1756 (2004).
13. B. A. Standish, V. X. D. Yang, N. R. Munce, L. M. Wong Kee Song, G. Gardiner, A. Lin, Y. I. Mao, A. Vitkin, N. E. Marcon, and B. C. Wilson, "Doppler optical coherence tomography monitoring of microvascular tissue response during photodynamic therapy in an animal model of Barrett's esophagus," Gastrointest. Endosc. **66**(2), 326–333 (2007).
14. A. Mariampillai, B. A. Standish, E. H. Moriyama, M. Khurana, N. R. Munce, M. K. K. Leung, J. Jiang, A. Cable, B. C. Wilson, I. A. Vitkin, and V. X. D. Yang, "Speckle variance detection of microvasculature using swept-source optical coherence tomography," Opt. Lett. **33**(13), 1530–1532 (2008).
15. S. A. Boppart, B. E. Bouma, C. Pitris, G. J. Tearney, J. G. Fujimoto, and M. E. Brezinski, "Forward-imaging instruments for optical coherence tomography," Opt. Lett. **22**(21), 1618–1620 (1997).
16. X. M. Liu, M. J. Cobb, Y. C. Chen, M. B. Kimmey, and X. D. Li, "Rapid-scanning forward-imaging miniature endoscope for real-time optical coherence tomography," Opt. Lett. **29**(15), 1763–1765 (2004).
17. Y. L. Wang, M. Bachman, G. P. Li, S. G. Guo, B. J. F. Wong, and Z. P. Chen, "Low-voltage polymer-based scanning cantilever for in vivo optical coherence tomography," Opt. Lett. **30**(1), 53–55 (2005).
18. X. D. Li, S. Martin, C. Pitris, R. Ghanta, D. L. Stamper, M. Harman, J. G. Fujimoto, and M. E. Brezinski, "High-resolution optical coherence tomographic imaging of osteoarthritic cartilage during open knee surgery," Arthritis Res. Ther. **7**(2), R318–R323 (2005).
19. C. P. Liang, J. Wierwille, T. Moreira, G. Schwartzbauer, M. S. Jafri, C. M. Tang, and Y. Chen, "A forward-imaging needle-type OCT probe for image guided stereotactic procedures," Opt. Express **19**(27), 26283–26294 (2011).
20. B. A. Standish, K. K. C. Lee, X. Jin, A. Mariampillai, N. R. Munce, M. F. G. Wood, B. C. Wilson, I. A. Vitkin, and V. X. D. Yang, "Interstitial Doppler optical coherence tomography as a local tumor necrosis predictor in photodynamic therapy of prostatic carcinoma: an in vivo study," Cancer Res. **68**(23), 9987–9995 (2008).
21. N. R. Munce, G. A. Wright, A. Mariampillai, B. A. Standish, M. K. K. Leung, L. Tan, K. Lee, B. K. Courtney, A. A. Teitelbaum, B. H. Strauss, I. A. Vitkin, and V. X. D. Yang, "Doppler optical coherence tomography for interventional cardiovascular guidance: in vivo feasibility and forward-viewing probe flow phantom demonstration," J. Biomed. Opt. **15**(1), 011103 (2010).
22. D. Overbay and L. Criddle, "Mastering temporary invasive cardiac pacing," Crit. Care Nurse **24**(3), 25–32 (2004).
23. C. Pizzanelli, R. Galli, F. S. Giorgi, A. Iudice, E. Bonanni, V. Pelliccia, S. Jensen, L. Manca, B. Lenzi, L. Lutzemberger, G. Parenti, F. Fornai, and L. Murri, "Vagus nerve stimulation as a treatment for refractory epilepsy: a 15-year experience in an Italian tertiary-care epilepsy center," Lett. Drug Des. Discov. **8**, 321–329 (2011).
24. J. D. Carlson, D. R. Cleary, J. S. Cetas, M. M. Heinricher, and K. J. Burchiel, "Deep brain stimulation does not silence neurons in subthalamic nucleus in Parkinson's patients," J. Neurophysiol. **103**(2), 962–967 (2010).
25. N. R. Munce, A. Mariampillai, B. A. Standish, M. Pop, K. J. Anderson, G. Y. Liu, T. Luk, B. K. Courtney, G. A. Wright, I. A. Vitkin, and V. X. D. Yang, "Electrostatic forward-viewing scanning probe for Doppler optical coherence tomography using a dissipative polymer catheter," Opt. Lett. **33**(7), 657–659 (2008).
26. C. Sun, K. K. C. Lee, B. Vuong, M. Cusimano, A. Brukson, A. Mariampillai, B. A. Standish, and V. X. D. Yang, "Neurosurgical hand-held optical coherence tomography (OCT) forward-viewing probe," Proc. SPIE **8207**, 82074V (2012).
27. V. X. D. Yang, M. L. Gordon, A. Mok, Y. H. Zhao, Z. P. Chen, R. S. C. Cobbold, B. C. Wilson, and I. A. Vitkin, "Improved phase-resolved optical Doppler tomography using the Kasai velocity estimator and histogram segmentation," Opt. Commun. **208**(4-6), 209–214 (2002).
28. S. Oyre, S. Ringgaard, S. Kozerke, W. P. Paaske, M. Erlandsen, P. Boesiger, and E. M. Pedersen, "Accurate noninvasive quantitation of blood flow, cross-sectional lumen vessel area and wall shear stress by three-dimensional paraboloid modeling of magnetic resonance imaging velocity data," J. Am. Coll. Cardiol. **32**(1), 128–134 (1998).

1. Introduction

Pituitary adenomas account for 10%–15% of all diagnosed intracranial tumors and the diagnosed cases are suggested to be increasing with the use of modern imaging techniques [1]. A mean prevalence of 94 cases per 100,000 population has been reported [2]. Subarachnoid hemorrhage (SAH) caused by a cerebral aneurysm that ruptures occurs in about 40–50 per 100,000 people over age 30 [3]. Both pituitary tumor and aneurysm can be operated on using modern microsurgical techniques through open craniotomy and minimally invasive surgeries

#165607 - $15.00 USD Received 3 Apr 2012; revised 7 May 2012; accepted 8 May 2012; published 16 May 2012

such as endovascular aneurysm treatment and transsphenoidal pituitary removal [4,5]. A significant number of aneurysms are surgically clipped, where small metallic clips are placed along the neck of the aneurysm to prevent blood from entering the aneurysm sac. Intraoperative micro-Doppler ultrasonography (MDU) probes are used to verify proper clip [6,7]. Pituitary tumors are commonly treated via endonasal transsphenoidal surgery, which goes directly through the back of the nose to reach the pituitary tumor [8,9]. Similar ultrasound Doppler probe are also used for pituitary removal guidance [10]. Although the Doppler ultrasound probes have been proven to physically fit the surgical environment and are able to reduce the surgical complications, they can only provide acoustic signal and lack structural imaging capabilities and visual feedback mechanisms to guide the surgical procedure. Furthermore, Doppler signal alone cannot precisely determine the depth of the internal carotid artery (ICA) that is completely encased by the pituitary tumor. If the ICA or its branches are not clearly identified during an open craniotomy or transsphenoidal procedure, there is a risk for catastrophic surgical related complications. During these surgical procedures, a probe that can provide detailed information of the microstructure and local hemodynamics could further reduce surgical complications.

Optical coherence tomography (OCT) [11,12] has been successfully used in pre-clinical and clinical applications due to its ability to resolve high-resolution structural and microvascular in real time [13,14]. Various probes have been developed to perform OCT imaging where the scanning mechanisms have been based on piezoelectric cantilever scanning through a GRIN lens [15,16], electroactive polymer cantilever [17] and scanning mirrors [18,19]. These designs may be optimal for applications such as mouth and skin imaging, and open knee surgery guidance. However, they are not suitable in the field of neurosurgery due to large distal-end (>3 mm), small field of view (<1 mm) or short length to reach pituitary tumors and cerebral aneurysms, which occur near the center of the head, at the skull base. In this paper, a handheld OCT imaging probe with the identical bayonet form factor of the clinically accepted non-imaging Doppler ultrasound probe is developed based on our previous successful development of blood flow detection image processing techniques [20] and forward-viewing OCT imaging mechanisms [21]. With the handheld bayonet form factor, OCT can be used to image internal tissue microstructures that was previously unavailable to surgeons, thus it may become a powerful imaging technology for surgery guidance.

2. Probe design and technical performance

2.1. Design

The OCT probe was developed for the conditions of intraoperative use. Its electrical source has extremely low current output, which is approximately 3 orders of magnitude less than typical current encountered during invasive cardiac pacing (~10 mA) [22], vagal nerve stimulation (~3 mA) [23], or deep brain stimulation (3~5 mA) [24]. In addition, it is relatively easy to sterilize and maintains a small instrument diameter for insertion through small incisions during minimally invasive surgical procedures. The probe incorporates an electrostatic forward viewing OCT scanner [21,25] into the familiar form factor of the Bayonet shape as shown in Fig. 1. (a). The internal scanning components at the distal end of the probe are displayed in Fig. 1(b), showing the geometries of the components and highlighting the scanning mechanism. GRIN lens with diameter of 1.8 mm (GRINTECH, Germany) is fit in a 2 mm outer diameter rigid tube. The outer diameter of the outer tube is 2.8 mm to fit with the Bayonet handle. The scanning section includes the GRIN lens, two wires, and a platinum coil going over an optical fiber. Mineral oil is filled in the tube to matchthe refractive index between the fiber and the GRIN lens. The two wires are connected to a DC high voltage (HV) power supply. When a certain voltage is applied (normally between 1200 V and 2500V), the fiber carried by the coil oscillates between the two wires, which enables 2D scan. Although the voltage is high, the current output is limited to a

#165607 - $15.00 USD Received 3 Apr 2012; revised 7 May 2012; accepted 8 May 2012; published 16 May 2012

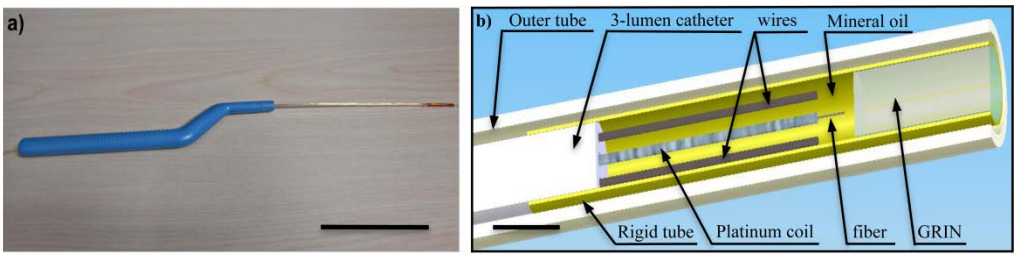

Fig. 1. (a) A photograph of the OCT handheld probe (scale bar represents: 100 mm). (b) A schematic drawing of the distal section of the probe showing the main parts for optical scanning (scale bar represents: 2mm).

maximum of 2 µA. Furthermore, the two electrical wires are insulated except the ~8 mm section extruding from the 3-lumen catheter, which are safely enclosed with nonconductive mineral oil and rigid tube. It is key to stress that the use of nonconductive material constitutes crucial principle of this device's operation based on electrostatic forces. Prior to in-vivo testing with human patients, it would be reasonable to subject the probe to further destructive tests to confirm the failure mode of the device will not involve sudden surge of output current, transient or permanent, and fully limited by the upper bound of the power source driving the probe.

2.2. Technical performance

For an OCT imaging probe, the optical characteristics, i.e. working distance (focal distance from the surface of the GRIN lens), depth of field (twice of the Raleigh range), and spot size (waist diameter), directly determine the properties of imaging such as image location, depth, and resolution [26]. The lateral scanning rate and linearity of the scanning determine the imaging stability. These parameters of the probe are described below.

2.2.1. spot size, working distance and field of view (FOV)

There is a tradeoff between the spot size, the working distance and FOV. ZEMAX simulation was used to optimize the design based upon these parameters. When the spot size is defined as the parameter to be optimized in ZEMAX simulation, the results demonstrate a minimum spot size of 13.8 µm, a working distance of 2.8 mm and a FOV radius of 2 mm when the distance between the fiber and the GRIN is 0.74 mm. A greater working distance and FOV is often desired. As a result, a series of simulations were conducted by changing the distance between the fiber tip and the GRIN surface from 0.05 mm to 0.8 mm. The simulation results are listed in Table 1. The spot size, working distance and the radius of FOV changes with respect to the distance between the fiber tip and the GRIN lens are plotted in Fig. 2(a). For each of the three plots, the vertical axis represents spot size, working distance and the radius of FOV, respectively, with the specific unit shown on the graph. During fabrication, the fiber tip was arranged at ~0.3-0.4 mm to the GRIN lens such that the probe had an approximately 20 µm spot size. Due to variance in the manual fabrication process, these parameters may have a

Table 1. ZEMAX simulation [20]

Distance (fiber to GRIN, mm)	Spot size (µm)	Working distance (mm)	FOV (mm)
0.05	55.9	12.9	8.4
0.1	43.2	10.4	6.8
0.2	29.4	7.4	5
0.3	22.4	5.7	3.8
0.4	18.4	4.6	3.2
0.5	16.1	3.9	2.6
0.6	14.7	3.3	2.4
0.7	14.1	2.9	2
0.8	13.8	2.6	1.8

#165607 - $15.00 USD Received 3 Apr 2012; revised 7 May 2012; accepted 8 May 2012; published 16 May 2012

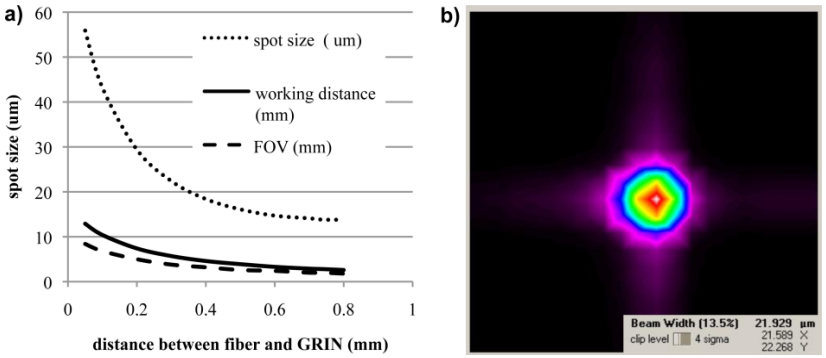

Fig. 2. Optical performance of the probe. (a) Probe imaging parameters vs. distance between fiber and GRIN. (b) Beam profile of the probe showing ~22 µm beam width [20].

slight tolerance for each individual probe. The beam profiles of probes were captured with a beam profiler (BP109-IR, Thorlabs). The beam profile of one of the probes is shown in Fig. 2 (b), which measured a $1/e^2$ spot size of ~22 µm. Based on Gaussian beam theory, the depth of focus is equal to twice of the Rayleigh range, which is ~1.16 mm with a wavelength of 1310 nm.

2.2.2. Scanning frequency

The scanning of the fiber in air was first tested with an applied voltage of 2000 V. A high-speed camera was used to record the motion of the fiber between the two wires and, software written in Labview 2009 was used to track the movement of the tip of the fiber. A video of the optical fiber oscillating between the two wires in air is shown in Fig. 3(a). The wire on the top is connected to the high voltage (HV) and the wire on the bottom is connected to the ground (GND) leads of a power supply. A plot of the displacement of the fiber tip versus time is shown in Fig. 3(b), with a scanning frequency of 130 Hz and a nearly linear scanning pattern. When the probe was immersed in mineral oil and a GRIN lens is attached to the distal end, the scanning frequency was decreased due to the viscosity of the mineral oil. The scanning frequency of the probe working at 2000 V was evaluated using an image correlation method described in section 3.1. The scanning frequency of the probe is determined by the length of the optical fiber, the mass of the optical fiber and platinum coiled wire surrounding the fiber, the viscosity of the mineral oil and the applied voltage. Nigel *et al.* [25] have given frequency response as a function of applied voltage of our previous prototype of electrostatic driven intravascular probe. For a spot size of 22 mm, the simulated working distance would be 5.7 mm and the FOV would be 3.8 mm. These are consistent with the measured values of 5 mm and 4 mm, respectively, as demonstrated in Fig. 3(c), a video of the probe scanning a ruler (Media 2). This corresponds to the 0.3 mm distance between the fiber tip and the GRIN from the simulation results. Small variations between the simulated and the measured values could

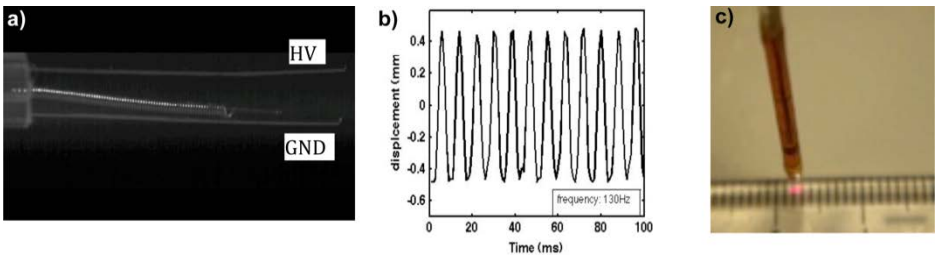

Fig. 3. (a) Motion of the optical fiber in air (scale bar represents 1 mm) (Media 1). (b) The displacement of the fiber tip in 100 ms. (c) A video of the probe scanning a ruler (Media 2), which shows ~5 mm working distance and ~4 mm FOV (scale bar represents 5 mm).

#165607 - $15.00 USD Received 3 Apr 2012; revised 7 May 2012; accepted 8 May 2012; published 16 May 2012

be attributed to discrepancies in the refractive indices used in the simulation and the actual value.

During scanning motion, the coil comes into contact with the ground wire resulting in an electrical discharge. This electrical pulse is then used to generate a frame trigger signal by an in-house built custom circuit. With the frame trigger, the frame rate of imaging can be controlled together with adjusting the line density of OCT scanning. If the frame rate of the OCT system is set exactly the same as the probe scanning frequency, both the forward (from GND to HV) and reverse scans (from HV to GND) will be recorded in each frame of OCT image. If the frame rate of the OCT system is twice of the probe scanning rate, only the forward scan will be included in the OCT images while the reverse scans are omitted, which is the imaging condition that we employed. This is described in more detail in section 3.1. Overall, if the frame rate of the OCT system is set faster than the probe scanning frequency, only a portion of the scanned region will be imaged.

3. Feasibility testing of the handheld probe for OCT imaging

The probe has been designed to be independent from OCT system, where the probe itself is simply connected to the sample arm. A schematic diagram of the probe connected to an OCT system is demonstrated in Fig. 4. The interference signal is measured by a balanced photodetector along with the clock signal and frame trigger signal, which are connected to data acquisition hardware (National Instruments).

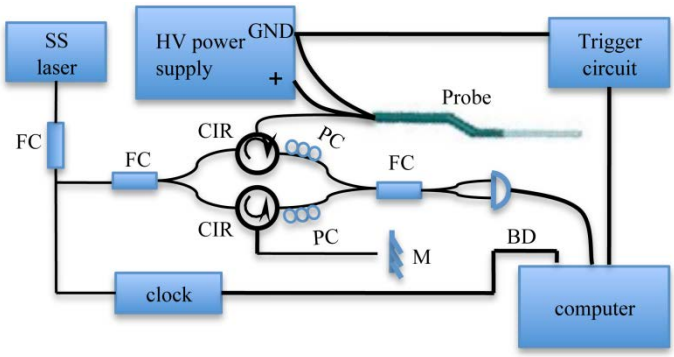

Fig. 4. Schematic diagram of a handheld probe with an OCT system. SS laser: swept source laser, FC: fiber coupler, CIR: circulator, PC: polarization controller, BD: balanced photodetector, M: mirror [20].

3.1. Imaging consistency test

In this test, the swept source laser utilized, in combination with the probe, was the Thorlabs SSOCT system (Thorlabs, USA) with an A-line scanning rate of 16 kHz (bidirectional) centered at 1310 nm. To evaluate the scanning frequency and imaging consistency, the probe was held steadily and repeated scans were captured in this one location. These repeated patterns are then analyzed by cross correlation. An image of an IR card taken by the probe at a frame rate of 2 frames/s and 2000V is shown in Fig. 5(a). A small region shown in the red rectangle was then chosen as the reference for correlation analysis. 26 correlation peaks were obtained from the correlation result shown in Fig. 5(b). The 26 repeated scans occurred in half a second, resulting in a scanning rate of 52 Hz. The distances between adjacent correlation peaks were constant with a variance of less than 5 pixels, which demonstrates the imaging consistency of the probe. When the forward and reverse scans follow the same trajectory, mirror images will be captured. However, imperfections during fabrication, coupled with the vibrations encountered (see Fig. 3), contribute to the hysteresis of the scanning motion since the two electrodes may not remain parallel at all times. Such deviation from symmetry and higher order frequency vibrations can introduce non-linear artifacts to the forward and

#165607 - $15.00 USD Received 3 Apr 2012; revised 7 May 2012; accepted 8 May 2012; published 16 May 2012

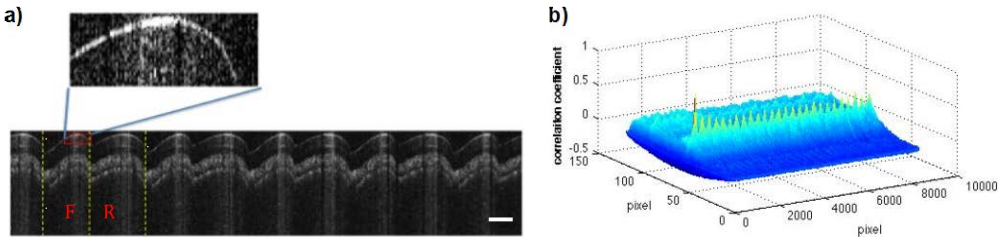

Fig. 5. Scanning frequency and imaging consistency evaluation. (a) part of a frame of an OCT image of an IR card taken at 2 frams/s. (b) Plot of the correlation coefficient showing 26 correlation peaks. The correlation was conducted between the small red rectangular area shown in (a) and the whole image.

backward scans. Thus, in Fig. 5(a), the forward scanning labeled as 'F' and reverse scanning labeled as 'R' show different patterns. At this situation, consistent B-mode imaging can be achieved by recording only the forward scans or reverse scans through the frame trigger control. Forward scans for image formation was elected in the following applications, and software signal processing was accomplished during the backward scan time.

3.2. Porcine femoral blood vessel imaging

To test the ability of the probe for both structural and blood flow *in vivo* imaging, a femoral blood vessel in the thigh of a hind leg of a Yorkshire pig (~50 Kg) was imaged by the handheld probe (protocol ACC307, approved by St. Michael's Hospital Animal Care and Use Committee, Toronto Canada). The probe was connected to a polygon-based SS-OCT system with sweeping frequency of 36kHz. During the procedure, the blood vessel was surgically exposed and the probe was held steadily to scan a cross-section of the blood vessel as shown in Figs. 6(a) and 6(b). In order to improve phase correlation for Doppler imaging, the probe was set at a slow scanning speed of ~20 Hz at a given voltage of 1600V. B-mode structural and Doppler images were recorded. A histogram-based velocity segmentation algorithm [27] was used to remove the artifacts induced by bulk motion including motion of the hand, vibration of the probe and the motion of the blood vessel. Figure 6(c) demonstrate a B-mode structural image of the blood vessel. The bulk motion is much slower compared to the imaging speed; therefore, its affect to structural imaging is trivial. Figure 6 =(d) (Media 3) shows the periodic Doppler shift induced by the blood flow over 5 seconds of imaging. A region of interest (ROI) was chosen, as shown in the white rectangle box in Fig. 6 =(d) and the average value within the ROI is calculated and plotted with time in Fig. 6 =(e). This plot clearly demonstrated the velocity change of the blood flow within a few cardiac cycles. Each frame of Fig. 6 =(d) (Media 3) further shows the hemodynamic pattern during the measured cardiac cycles, where the blood flow has greater velocity (Doppler shift) in the center of the vessel than along the vessel wall. The velocity profiles along a horizontal and a vertical line (dashed lines shown in Fig. 6 =(d)) are plotted in Figs. 6 =(f) and 6(g), where the dashed lines represent the Doppler shift obtained from OCT. The solid lines represent quadratic fittings, where it can be seen that the velocity profile takes on the shape of a parabola demonstrating a laminar flow mode [28]. Figure 6(g) shows a half parabola because only the top half of the cross-section of the blood vessel was imaged due to limited imaging penetration. Based on the velocity profile, vessel wall shear stress can be calculated.

#165607 - $15.00 USD Received 3 Apr 2012; revised 7 May 2012; accepted 8 May 2012; published 16 May 2012

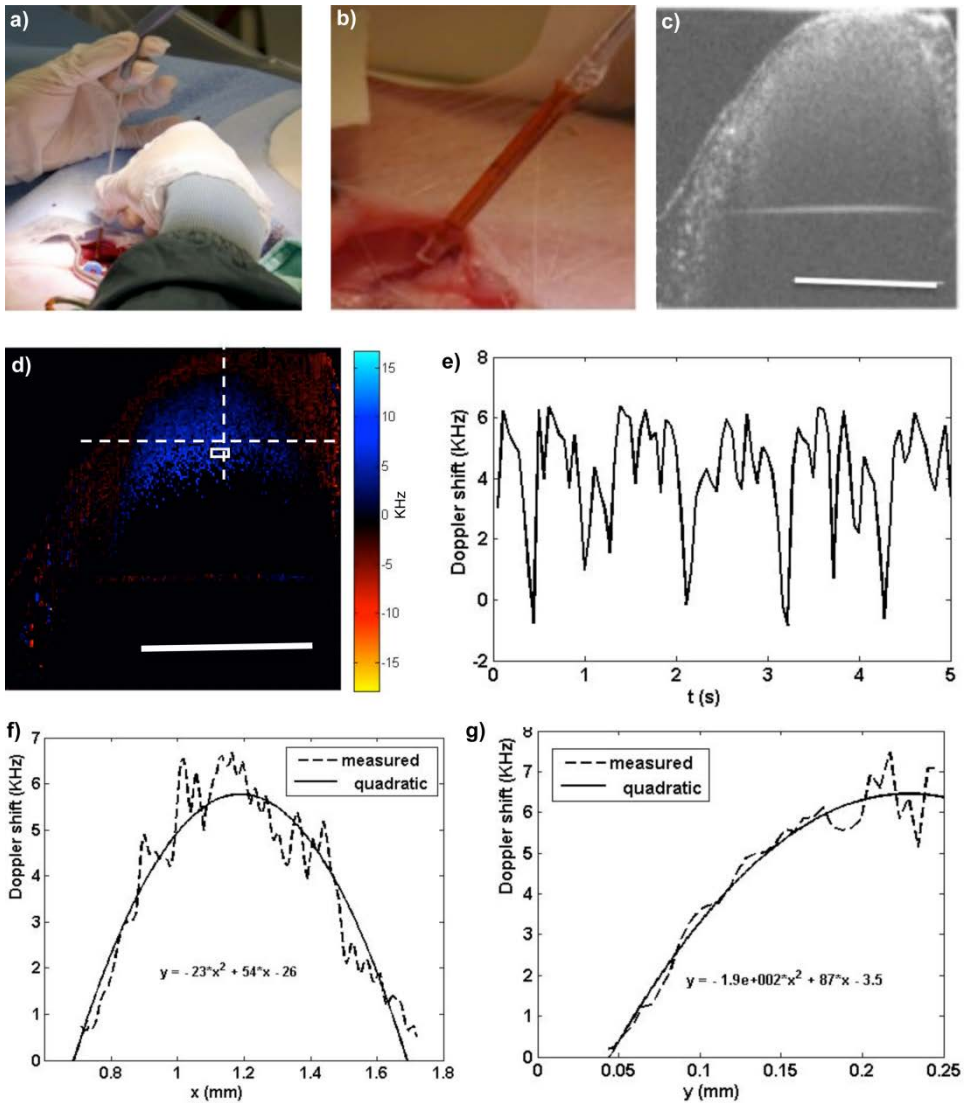

Fig. 6. Femoral artery imaging using the handheld probe. (a) A photograph of probe held for imaging. (b) The probe tip pointed to the exposed blood vessel. (c) A structural image of the blood vessel. (d) Doppler shift over ~5 s demonstrating the blood flow dynamics (Media 3). The white rectangle is the ROI. (Scale bars represent 1 mm) (e) The Doppler shift changes in 5 s calculated by averaging the values in the ROI. (f) Plot of the blood flow profile along the horizontal line shown in (d) at a certain time and its quadratic fitting curve (g) Plot of the blood flow profile along the vertical line in (d) its fitting curve.

4. Discussion and conclusion

A prototype OCT handheld probe was developed to obtain forward viewing images capable of both structural and Doppler images without the use of a complex lens and actuating system. For microsurgical use during the intended neurosurgery applications (e.g., cerebral aneurysms or pituitary tumors), we anticipate the probe will be used in a non-contact format. Considering one of the major complications of cerebral aneurysm surgery is rupture of the aneurysm, it may be ideal for the probe to be non-contact with the imaging target, which may have a thin wall. This is also one of the advantages of optical imaging over ultrasonic techniques, which necessitates liquid coupling agent. Furthermore, the ZEMAX simulation also indicates that if

#165607 - $15.00 USD Received 3 Apr 2012; revised 7 May 2012; accepted 8 May 2012; published 16 May 2012

the probe is in contact with tissue (index of refraction of approximately 1.38 or coupling agent such as water, 1.33), the effective scanning angle will be smaller given the same GRIN lens index profile. This is the second reason we chose a non-contact working condition. On the other hand, coupling gel with index matching may improve the optical transmission and reduce specular reflections on the OCT images. Therefore, there are signal-to-noise tradeoffs that we have made with the current design. The probe length was easily modified to fit the length between the surgeon's hands and the imaging target. The frame rate of the imaging probe was determined by both the scanning speed of the probe and the number of A-scans in each frame set for the OCT system. From Fig. 4, it can be seen that the tube itself oscillates with the fiber striking the wires and the movements of the fiber near the wires do not have very good linearity, which may affect the imaging. Stiffer tube and new tube designs will be implemented in the future to improve the robustness of the probe.

The probe offers high-resolution, depth resolved, blood vessel/anatomical layer detection as well as the ability to measure blood flow dynamics. Structural and Doppler images of a porcine femoral blood vessel demonstrate the intraoperative vascular imaging capability and feasibility. Moreover, Doppler OCT imaging of the mode of blood flow and endolumenal hemodynamics will enable the detection of blood flow and possible characterization of the spatial and temporal variation of the wall shear stresses associated with pulsatile flows, intraoperatively. A future objective of this OCT handheld probe includes real-time imaging during open craniotomy procedures for pituitary tumors, cerebral aneurysms and transsphenoidal neuroendoscopic treatment of pituitary tumors.

Acknowledgments

This work was supported by the Canadian Institutes of Health Research (CIHR), NSERC and CRC. The authors would like to thank Dr. Guillermo J. Tearney and Dr. Arthur Day for their fruitful discussions.

#165607 - $15.00 USD Received 3 Apr 2012; revised 7 May 2012; accepted 8 May 2012; published 16 May 2012